LAWRENCE
LIVERMORE
NATIONAL
LABORATORY

UCRL-JRNL-227180

Scaling the Incompressible Richtmyer-Meshkov Instability

D. Cotrell, A. Cook

January 11, 2007

Physics of Fluids

Scaling the Incompressible Richtmyer-Meshkov Instability

David L. Cotrell and Andrew W. Cook
Lawrence Livermore National Laboratory
Livermore, CA 94550, USA
(Dated: January 9, 2007: to be submitted to *Physics of Fluids*)

We derive a scaling relation for Richtmyer-Meshkov instability of incompressible fluids. The relation is tested using both numerical simulations and experimental data. We obtain collapse of growth rates for a wide range of initial conditions by using vorticity and velocity scales associated with the interfacial perturbations and the acceleration impulse. A curve fit to the collapsed growth rates yields a fairly universal model for the mixing layer thickness versus time.

In this work, we consider the incompressible Richtmyer-Meshkov (RM) instability of an impulsively accelerated interface separating two fluids of different density [1, 2]. This instability is of fundamental importance in a variety of applications spanning a wide range of length scales. At large scales RM instability generates mixing in supernovae [3, 4]; at smaller scales it enhances mixing in ramjet engines [5]; at even smaller scales it initiates shell break-up in inertial confinement fusion capsules [6, 7]. The initial evolution of RM instabilities can be described in terms of vortex dynamics. Zabusky and others [8, 9] have discussed the crucial role vorticity plays in the early development of RM and other baroclinic instabilities. In this Brief Communication, we demonstrate that characteristic vorticity and velocity scales, derived from the impulse and initial conditions, lead to collapse of mixing layer growth rates over a broad parameter space.

The conservation laws governing RM instability between two incompressible miscible fluids in a Cartesian frame of reference are [10]:

$$\frac{\partial \rho Y_m}{\partial t} + \frac{\partial \rho Y_m V_j}{\partial x_j} = \frac{\partial}{\partial x_j}\left(\rho D \frac{\partial Y_m}{\partial x_j}\right) \quad , \quad (m = 1, 2) \tag{1}$$

$$\frac{\partial \rho V_i}{\partial t} + \frac{\partial \rho V_i V_j}{\partial x_j} = -\frac{\partial P}{\partial x_i} + \frac{\partial \tau_{ij}}{\partial x_j} + \rho g_i \quad , \tag{2}$$

where

$$\tau_{ij} = \mu\left[\frac{\partial V_i}{\partial x_j} + \frac{\partial V_j}{\partial x_i} - \frac{2}{3}\delta_{ij}\frac{\partial V_k}{\partial x_k}\right] \quad . \tag{3}$$

Here, ρ is the mixture density, Y_m is the mass fraction of species m, $V_i = (V_x, V_y, V_z)$ is the mass-averaged mixture velocity, P is the pressure, D is the Fickian diffusivity, μ is the dynamic viscosity, and g_i is the acceleration. Our goal is to derive a model for the rate of growth of the mixing region, given a functional form for g_i and a known set of initial conditions. The width of the RM mixing region is defined in terms of entrained mole fractions. The mole fraction of heavy fluid is

$$X = \frac{\rho - \rho_1}{\rho_2 - \rho_1} \quad , \tag{4}$$

(where ρ_1 and ρ_2 are the densities of the light and heavy fluids, respectively) and the mole fraction of mixed fluid is

$$X_m(X) = \begin{cases} 2X & \text{if } X \le 1/2 \\ 2(1-X) & \text{if } X > 1/2 \end{cases} \quad . \tag{5}$$

Using (4) and (5), the mixing layer thickness is defined as

$$h \equiv \int_{-\infty}^{\infty} X_m(\langle X \rangle)\, dz \quad , \tag{6}$$

where the angle brackets, $\langle\rangle$, denote an xy-average, taken parallel to an interface located at $z = 0$. The rate of growth of the mixing region is then $\dot{h} = \partial h/\partial t$.

The net vorticity in the mixing region is

$$\Omega(t) = \frac{1}{l_x l_y l_z}\int_{-l_z/2}^{l_z/2}\int_0^{l_y}\int_0^{l_x} ||\boldsymbol{\omega}(\boldsymbol{x}, t)||\, \mathrm{d}x\, \mathrm{d}y\, \mathrm{d}z \quad , \tag{7}$$

where $\boldsymbol{\omega}$ is the vorticity vector, l_x and l_y are the horizontal dimensions of the flow domain, and l_z is the z-extent of the rotational fluid. Similarly, the root-mean-square (rms) velocity is

$$V'(t) = \left[\frac{1}{l_x l_y l_z}\int_{-l_z/2}^{l_z/2}\int_0^{l_y}\int_0^{l_x} ||\boldsymbol{V}(\boldsymbol{x}, t)||^2\, \mathrm{d}x\, \mathrm{d}y\, \mathrm{d}z\right]^{1/2} . \tag{8}$$

If t_s is the time-duration of the impulse, then $\Omega_s = \Omega(t_s)$ and $V_s = V'(t_s)$ correspond to the net vorticity and speed generated by the impulse, respectively. An expression for Ω_s can be derived from the vorticity equation,

$$\frac{\partial \boldsymbol{\omega}}{\partial t} + \boldsymbol{\nabla} \times (\boldsymbol{\omega} \times \boldsymbol{V}) = \frac{1}{\rho^2}\boldsymbol{\nabla}\rho \times \boldsymbol{\nabla} P + \boldsymbol{\nabla} \times \left(\frac{1}{\rho}\boldsymbol{\nabla} \cdot \tau_{ij}\right) , \tag{9}$$

by assuming quiescent flow during the impulse. For

the studies herein, the impulse takes the form

$$\boldsymbol{g}(t) = \begin{cases} (0,0,-G\sin(t)) & \text{if } t \le \pi \\ (0,0,0) & \text{if } t > \pi \end{cases} , \tag{10}$$

hence $t_s = \pi$. By further assuming a hydrostatic pressure gradient, i.e., $\frac{\partial P}{\partial x} = \frac{\partial P}{\partial y} = 0$, and $\frac{\partial P}{\partial z} = \rho g_z$ for $0 \le t \le t_s$, (9) reduces to

$$\frac{\partial \omega_x}{\partial t} = \frac{1}{\rho^2}\frac{\partial \rho}{\partial y}\frac{\partial P}{\partial z} = -G\sin(t)\frac{1}{\rho}\frac{\partial \rho}{\partial y} \tag{11}$$

$$\frac{\partial \omega_y}{\partial t} = \frac{-1}{\rho^2}\frac{\partial \rho}{\partial x}\frac{\partial P}{\partial z} = G\sin(t)\frac{1}{\rho}\frac{\partial \rho}{\partial x} \tag{12}$$

$$\frac{\partial \omega_z}{\partial t} = 0 \quad . \tag{13}$$

Taking the density variation in the layer during the impulse to be time-invariant and integrating (11-13) over $0 \le t \le t_s$, together with the initial condition $\boldsymbol{\omega}(\boldsymbol{x}, 0) = 0$, yields

$$\omega_x(\boldsymbol{x}, t_s) = -2G\frac{1}{\rho}\frac{\partial \rho}{\partial y} \tag{14}$$

$$\omega_y(\boldsymbol{x}, t_s) = 2G\frac{1}{\rho}\frac{\partial \rho}{\partial x} \tag{15}$$

$$\omega_z(\boldsymbol{x}, t_s) = 0 \quad . \tag{16}$$

In the simulations herein, the initial density distribution takes the form

$$\rho(\boldsymbol{x}, 0) = \frac{1}{2}\left[\rho_2 + \rho_1 + (\rho_2 - \rho_1)\text{erf}\left(\frac{2z}{\delta} + \epsilon\xi(x,y)\right)\right], \tag{17}$$

where δ is the initial thickness of the diffusion zone, $\xi(x, y)$ describes the interfacial perturbations and ϵ is a dimensionless disturbance amplitude. We obtain $\boldsymbol{\omega}$ by plugging (17) into (14-16) and subsequently compute Ω_s from (7). The Biot-Savart law is then used to calculate the velocity vector,

$$\boldsymbol{V} = \frac{1}{4\pi}\int \boldsymbol{\omega}(\bar{\boldsymbol{x}}, t_s) \times \frac{(\boldsymbol{x} - \bar{\boldsymbol{x}})}{||\boldsymbol{x} - \bar{\boldsymbol{x}}||^3}\, \mathrm{d}\bar{x}\, \mathrm{d}\bar{y}\, \mathrm{d}\bar{z} \quad , \tag{18}$$

at which point $\boldsymbol{V}$ is inserted into (8) to obtain V_s. Thus, given functional forms for $\xi(x, y)$ and g_z, characteristic vorticity and velocity scales (Ω_s & V_s) can be obtained analytically.

In order to evaluate the validity of the static-flow approximations discussed above, analytical expressions (denoted Ω_s^a & V_s^a) are compared to numerical values computed from simulation data (denoted Ω_s^c & V_s^c). In the simulations, (1) and (2) are solved with a hybrid spectral-Padé scheme for spatial derivatives, combined with a predictor-corrector pressure-projection method for temporal integration. Verification and validation tests of the numerical algorithm were previously reported [10, 11]. Dimensional variables are normalized by the grid spacing, Δ, the light fluid density, ρ_1, and the acceleration magnitude, G; i.e., $\Delta = \rho_1 = G = 1$. Setting $\rho_2 = 3$, $\delta = 4$, $\epsilon = 0.2$ and $\xi(x, y) = \left[\cos(\frac{2\pi x}{l_x}) + \cos(\frac{2\pi y}{l_y})\right]$, we find: $\Omega_s^c = 3.3 \times 10^{-4}$, $\Omega_s^a = 3.4\times10^{-4}$, $V_s^c = 1.0\times10^{-2}$ and $V_s^a = 9.3\times10^{-3}$. Increasing δ from 4 to 8 results in $\Omega_s^c = 6.6 \times 10^{-4}$, $\Omega_s^a = 6.9\times10^{-4}$, $V_s^c = 2.0\times10^{-2}$ and $V_s^a = 1.8\times10^{-2}$. If the impulse is reversed, i.e., $G = -1$ instead of 1, Ω_s^a remains unchanged while Ω_s^c decreases by about 2%. This decrease is expected due to the fact that, when the pulse is directed from light to heavy fluid, the perturbations invert before the layer begins to grow. Differences between analytical and numerical values for Ω_s and V_s are small; hence, the quasi-static assumptions made in determining Ω_s^a and V_s^a appear reasonably valid, provided the impulse is sufficiently quick, such that the layer grows very little during the impulse. Furthermore, our results indicate that collapse of growth rates does not depend on whether analytical or numerical values are used to scale the data.

Since $1/\Omega_s$ and V_s ought to provide natural time and velocity scales for any RM flow, we expect $\dot{h}(t\Omega_s)/V_s$ to be a fairly universal function. As a first test of this hypothesis, our scaling is applied to the experimental results of Niederhaus and Jacobs [7], where we have used second-order central differences to calculate $\dot{h}$ from their mixing layer data (figure 1a). These experiments were conducted with miscible fluids at low Atwood number using a 3 m drop tower and sled apparatus. Perturbations were imposed on the density interface by gently oscillating the tank horizontally to produce $n + 1/2$ standing internal waves. In the present work, experimental results are shown for $n = 1$, an Atwood number of $A \equiv (\rho_2 - \rho_1)/(\rho_2 + \rho_1) = 0.16$, and six initial disturbance amplitudes. As can be seen in figure 1b, the current scaling does an excellent job of collapsing the data.

As a second test of the effectiveness of our scaling, computational results are shown for $\dot{h}$ versus time for various combinations of the parameters ρ_2, ϵ, k_p, and σ. In the simulations, k_p is the peak wavenumber of a Gaussian perturbation spectrum with standard deviation σ. Unless otherwise noted, all computational results discussed below are for multi-mode disturbances such as those used in [10], a domain size of 256^3, $l_z/2 = 4\delta(1 + \epsilon)$, $\delta = 4$, and $\sigma = 2$. Owing to the broad-bandedness of the initial density disturbance, the numerical results are scaled using Ω_s^c and V_s^c.

Figure 2 shows unscaled and scaled mixing layer

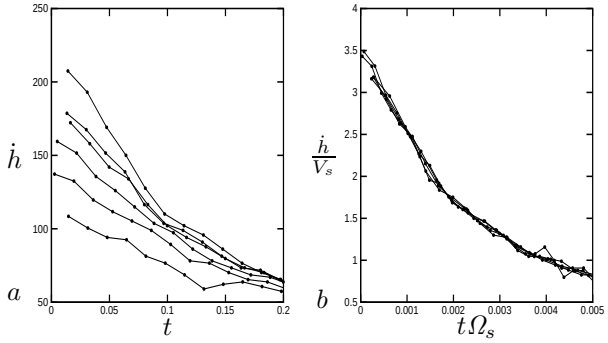

FIG. 1: Unscaled and scaled mixing layer growth rates computed from the experimental data of Niederhaus & Jacobs (*J. Fluid Mech.*, **485**, 2003, p. 243).

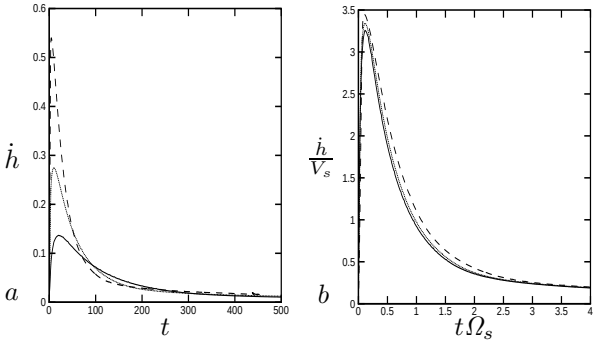

FIG. 3: Unscaled and scaled mixing layer growth rates for $A = 0.5$, $k_p = 16$, and $\epsilon = 0.2$ (solid), 0.4 (dotted), and 0.8 (dashed).

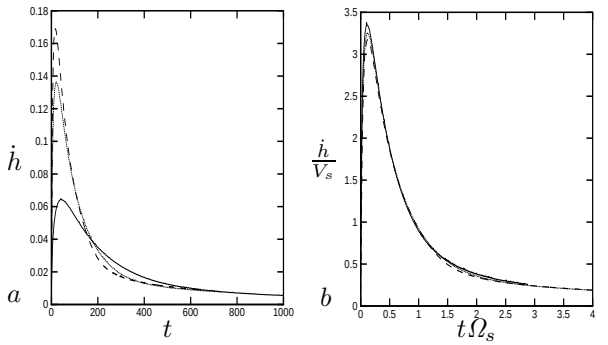

FIG. 2: Unscaled and scaled mixing layer growth rates for $k_p = 16$, $\epsilon = 0.2$, and $A = 0.25$ (solid), 0.5 (dotted), and 0.6 (dashed).

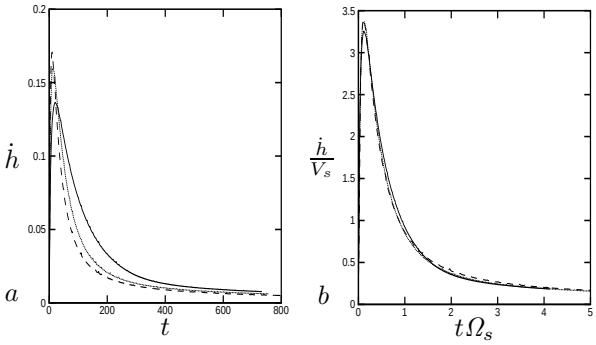

FIG. 4: Unscaled and scaled mixing layer growth rates for $A = 0.5$, $\epsilon = 0.2$, and $k_p = 16$ (solid), $k_p = 24$ (dotted), and 32 (dashed).

growth rates for $k_p = 16$ and $\epsilon = 0.2$ with $A = 0.25$, 0.5 and 0.6. There are significant differences between the mixing layer growth rates at early and intermediate times; i.e., the peaks are widely disparate and somewhat out of phase. On a side note, the differences between peaks appear to decrease with increasing Atwood number. The maximum difference between peak growth rates is about 61% (figure 2a); whereas, the maximum difference between peaks for the scaled growth rates is about 5% (figure 2b).

Figure 3 shows unscaled and scaled mixing layer growth rates for $A = 0.5$ and $k_p = 16$ with $\epsilon = 0.2$, 0.4 and 0.8. The unscaled peak growth rates are again out of phase, with roughly an 88% maximum difference between peaks (figure 3a). The scaled growth rates are in phase, with a maximum peak-to-peak difference of about 6% (figure 3b).

Figure 4 shows unscaled and scaled mixing layer growth rates for $A = 0.5$ and $\epsilon = 0.2$ with $k_p = 16$, 24 and 32. In this case the differences in the unscaled growth rates persist to very late time. The maximum difference between peak growth rates is about 60% (figure 4a) decreasing to about 6% when scaled (figure 4b).

We can evaluate empirical models for $\dot{h}$ using the scaled growth rate data (figures 2b, 3b and 4b). Beginning with a generalization of the model by Sadot et al. [12],

$$\frac{\dot{h}}{V_s} = \frac{a_1 \Omega_s t}{1 + a_2 \Omega_s t + a_3 (\Omega_s t)^b} \quad , \tag{19}$$

which has limiting behavior $\lim_{t\to 0} \dot{h} = 0$ and $\lim_{t\to\infty} \dot{h} \propto t^{1-b}$, we seek values for a_1, a_2, a_3 and b which best fit the data. Setting $b = 2$, as in the Sadot et al. model, and using least-squares we find $a_1 = 69.2$, $a_2 = 2.55$, and $a_3 = 71.7$. This model has difficulty capturing the entire growth history (red curve in figure 5). The constants can be adjusted to better capture either the peaks or late time growth rates but not both at once. A better fit is obtained by considering a range of b and choosing the value (2.37 in this case) that minimizes the rms difference between the model (for a given b) and the numerical

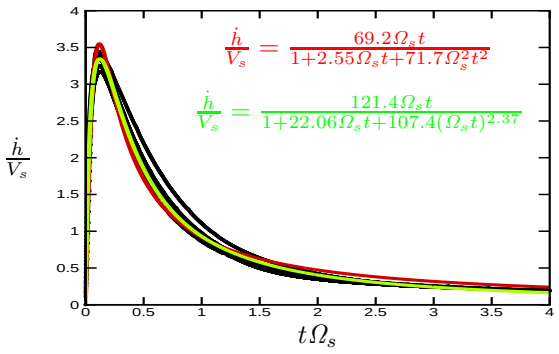

FIG. 5: Mixing layer growth data for the three numerical cases, color curves represent models based on data fitting.

data. The resulting curve fit does much better at predicting the mean growth rate of the collapsed data at early and intermediate times, while also capturing its asymptotic behavior (green curve in figure 5). This model constitutes an improvement over previous models [12–16] in that it is based on a fairly universal scaling, and as such, should be valid for single or multi-mode disturbances of arbitrary amplitude at both early and late times.

The authors would like to thank Prof. J. W. Jacobs for supplying the experimental data. This work was carried out under the auspices of the U.S. Department of Energy by the University of California Lawrence Livermore National Laboratory under Contract No. W-7405-ENG-48.

[1] R. D. Richtmyer. Taylor instability in shock acceleration of compressible fluids. *Commun. Pure Appl. Maths*, 13:297, (1960).

[2] E. E. Meshkov. Instability of the interface of two gases accelerated by a shock wave. *Izv. Akad. Nauk. SSSR Mekh. Zhid. i Gaza*, 4:151, (1969).

[3] W. D. Arnett, J. N. Bahcall, R. P. Kirshner, and S. E. Woosley. Supernova 1987a. *Annu. Rev. Astron. Astrophys.*, 27:629, (1989).

[4] A. Burrows, J. Hayes, and B. A. Fryxell. On the nature of core-collapse supernova explosions. *Astrophys. J.*, 450:830, (1995).

[5] E. Curran, W. Heiser, and D. Pratt. Fluid phenomena in scramjet combustion systems. *Annu. Rev. Fluid Mech.*, 28:323, (1996).

[6] J. D. Lindl. Development of the indirect-drive approach to inertial confinement fusion and the target physics basis for ignition and gain. *Phys. Plasmas*, 2:3933, (1995).

[7] C. E. Niederhaus and J. W. Jacobs. Experimental study of the Richtmyer-Meshkov instability of incompressible fluids. *J. Fluid Mech.*, 485:243, (2003).

[8] N. J. Zabusky. Vortex paradigm for accelerated inhomogeneous flows: Visiometrics for the Rayleigh-Taylor and Richtmyer-Meshkov environments. *Annu. Rev. Fluid Mech.*, 31:495, (1999).

[9] D. K. Lee, G. Peng, and N. J. Zabusky. Circulation rate of change: A vortex approach for understanding accelerated inhomogeneous flows through intermediate times. *submitted to Physics of Fluids.*, (2005).

[10] A. W. Cook, W. Cabot, and P. L. Miller. The mixing transition in Rayleigh-Taylor instability. *J. Fluid Mech.*, 511:333, (2004).

[11] A. W. Cook and P. E. Dimotakis. Transition stages of Rayleigh-Taylor instability between miscible fluids. *J. Fluid Mech.*, 443:69, (2001).

[12] O. Sadot, L. Erez, U. Alon, D. Oron, L. A. Levin, G. Erez, G. Ben-Dor, and D. Shvarts. Study of nonlinear evolution of single-mode and two-bubble interaction under Richtmyer-Meshkov instability. *Phys. Rev. Lett.*, 80:1654, (1998).

[13] Q. Zhang and S. Sohn. Non-linear theory of unstable fluid mixing driven by shock wave. *Physics of Fluids*, 9:1106, (1997).

[14] Q. Zhang and S. Sohn. Quantitative theory of Richtmyer-Meshkov instability in three dimensions. *ZAMP*, 50:1, (1999).

[15] D. Oron, L. Arazi, D. Kartoon, A. Rikanati, U. Alon, and D. Shvarts. Dimensionality dependence of the Rayleigh-Taylor and Richtmyer-Meshkov instability late-time scaliing laws. *Physics of Plasmas*, 8:2883, (2001).

[16] K. O. Mikaelian. Explicit expressions for the evolution of single-mode Rayleigh-Taylor and Richtmyer-Meshkov instabilities at arbitrary atwood numbers. *Phys. Rev. E*, 67:026319, (2003).